

Abstract

The shapes of mantle plumes are sensitive to mantle viscosity, density structure, and flow patterns. Increasingly, global tomographic models reveal broad plume conduits in the lower mantle and highly-tilting conduits in the mid and upper mantle. Previous studies mostly relied on 2D slices to analyze plume shapes, but fully investigating the complexity of 3D plume structures requires more effective visualization methods. Here, we use immersive headset-based virtual reality (VR) to visualize the full-waveform global tomographic models SEMUCB-WM1 and GLAD-M25. We develop criteria for the identification of plume conduits based on the relationship between the plume excess temperature and the V_S anomaly (δV_S). We trace 20 major plume conduits, measure the offsets of the conduits in azimuth and distance with respect to the hotspots, calculate the tilt angle, and evaluate the δV_S along all traced conduits. We compare our traced conduits with the conduits predicted by global mantle convection models and vertical conduits. The wavespeed variations along conduits traced from each tomographic model are slower than modeled or vertical conduits, regardless of which tomographic model they are evaluated in. The shapes of traced conduits tend to differ greatly from modeled conduits. Plume ponding and the emergence of secondary plumes, which could result from a combination of compositional variations, phase transitions, small-scale convection, and variations in viscosity, can contribute to the complex observed plume shapes. The variation of δV_S along the traced conduits and complex plume shapes suggest a thermochemical origin of many plumes.

1 Introduction

Deep mantle plumes originating from the Core Mantle Boundary (CMB) are thought to have a broad head, which generates Large Igneous Provinces (LIPs), and a narrower tail, which forms long-lived hotspots (e.g. Richards et al., 1989). The geochemical diversity of hotspot lavas, which are also known as Ocean Island Basalts (OIBs), reflects the entrainment and transport of different mantle materials by ascending plumes. Hence, understanding the shapes of mantle plumes is important for linking the rock record with deep mantle structures, including the Large Low Shear Velocity Provinces (LLSVPs) and Ultra Low Velocity Zones (ULVZs). Plume shape is influenced by the global pattern of mantle circulation as well as the intrinsic buoyancy and viscosity variations within ascending plumes and the ambient mantle. Seismic tomography is the only geophysical method that currently resolves plume-scale features at all mantle depths. Tomographic models shape our understanding of mantle plumes and naturally become a constraint on numerical models that aim to understand their structure and evolution. These comparisons bridge our theoretical models to tomographic images of mantle plumes and help advance our understanding of the physical and chemical properties of mantle plumes. Here we analyze the shapes of mantle plumes using immersive 3D visualization based on two recent global tomographic models and consider the implications of plume shape for the pattern of global mantle circulation and the variation of mantle viscosity.

Mantle plumes that rise to the surface have previously been described conceptually as primary and secondary plumes (Courtillot et al., 2003) on the basis of their buoyancy fluxes, upper mantle seismic signature, and the isotopic variations in OIBs. Primary plumes rise directly from the CMB, whereas secondary plumes rise from the superswells or broad primary plumes that pond below the upper mantle. State-of-art global tomographic models show patterns of slow shear velocity (V_s) resembling both types of plumes, although the plume shapes revealed by tomographic models have more complexities than what is proposed by the schematic plume model of Courtillot et al. (2003).

There has been considerable debate about whether hotspots are preferentially located at the edges of the Pacific and African LLSVPs (Torsvik et al., 2006; Steinberger & Torsvik, 2012) or whether they are associated with the LLSVP edges and interiors (Austermann

et al., 2014; Davies et al., 2015; Doubrovine et al., 2016). These two hypotheses have different geodynamics implications: whether plumes rise from the edge of the pile-like LLSVPs (Tan et al., 2011; Hassan et al., 2015), or the LLSVPs are cluster of plumes (Davaille & Romanowicz, 2020).

Two complementary approaches have been taken to understand the evolution of mantle plumes. First, some numerical models of thermal and thermochemical plume ascent focus on idealized plumes and incorporate a high degree of physical realism at the expense of describing the geologic context of specific plumes within Earth’s mantle (Dannberg & Sobolev, 2015; H. Liu & Leng, 2020). A second class of numerical models focuses on the influence of the global mantle flow associated with Earth’s tectonic history on plume conduits at the expense of a complete treatment of mantle rheology, phase transitions, and plume buoyancy (e.g., Steinberger & O’Connell, 1998). For the first class of studies, the comparison between the shape of the observed and the modeled plume conduits is only qualitative because idealized models do not attempt to reproduce the detailed dynamics of specific plumes. The second class of models does make testable predictions of plume shape that can be qualitatively and quantitatively compared with plumes resolved in tomographic models but only in terms of the wavespeed variations (Boschi et al., 2007).

Plume shapes depend on both the inherent properties of a plume and the surrounding mantle conditions, so they provide information about the composition and dynamics of plume and mantle. For example, the amount and direction of shear of plume conduits reflect the large-scale mantle flow pattern. Changes in the conduit radius could indicate the viscosity variations across the mantle. The stagnation of plumes helps to reveal the influence of the pressure-induced phase transitions on mantle convection. It is crucial to measure the shapes of plume conduits quantitatively to make more appropriate and meaningful connections between numerical models and tomographic observations.

Measuring plume shapes from tomographic models requires effective visualization of what are three-dimensional (3D) datasets, but most approaches to their visualization have involved two-dimensional (2D) slicing or the rendering of isosurfaces (surfaces defined by a constant value) on a 2D medium such as a computer screen or a paper (French & Romanowicz, 2015; Tsekhmistrenko et al., 2021; Celli et al., 2021). The understanding and insight gained from 2D visualizations of 3D data may be different than that gained through immersive 3D visualization. For example, the 2D cross-section of a plume cluster associated with the Pacific LLSVP seems to imply that the conduits of plume Samoa, and Tahiti are not resolved above 660 km depth (Figure 1a). However, the conduits of these plumes extend out of the vertical cross-section plane, as shown in Figure 1b. Selecting an isosurface with a specific negative δV_S to represent the boundary of a plume reveals plume shapes better than 2D cross sections and allows us to “see through” the non-negative δV_S that obscures our view. However, these approaches may fail if the shape of a plume is best represented by different isosurface values at different depths or when many plumes are clustered. In the first case, visualizing plumes requires observing the structures of many different δV_S isosurfaces simultaneously. In the second case, the isosurfaces representing boundaries of conduits usually obscure each other, making it tricky to identify an individual conduit if the observer is outside the cluster. This is the scenario for the plumes feeding Pitcairn, Macdonald, Marquesas, Tahiti, Samoa, and Easter, which are located close together within the Pacific LLSVP (Figure 2).

Visualizing seismic tomographic models in a virtual reality (VR) environment can help to overcome these barriers. Immersive visualization allows an observer to explore mantle structures from within and view them quickly from arbitrary vantage points. Immersive 3D visualization is not new in geoscience research but has not seen widespread adoption due to the lack of commodity VR hardware and related software. Previously, the usage of VR environments centered on large, immobile, and expensive “cave” environments (e.g., Billen et al., 2008). As VR headset devices have become more preva-

116 lent, immersive 3D visualization is becoming more accessible due to its lower cost and
 117 greater portability, presenting the potential to enable new discoveries.

118 The remainder of the paper is structured as follows. We establish a quantitative
 119 procedure to define mantle plume conduits and discuss the advantages and limitations
 120 of our conduit-choosing criteria. We present our traced conduits for well-resolved plumes
 121 in SEMUCB-WM1 (French & Romanowicz, 2014) and GLAD-M25 (V_S) (Lei et al., 2020)
 122 and the quantitative measurement of these conduits. We demonstrate that our traced
 123 conduits are more consistent with the distributions of slow seismic velocities than geo-
 124 dynamic model predictions. We discuss the implications and potential applications of
 125 this study.

126 2 Methods

127 The two tomographic models analyzed in this study, SEMUCB-WM1 and GLAD-
 128 M25, are state-of-art global tomographic models based on full waveform inversion (FWI).
 129 SEMUCB-WM1 inverts for 3-D variations in Voigt-average isotropic V_S and radial anisotropy
 130 parameter ξ and parameterizes them radially using (continuous) cubic b-splines and lat-
 131 erally using spherical splines. Its starting model is SEMum2 (French et al., 2013) above
 132 800 km and SAW24B16 (Méglin & Romanowicz, 2000) below. The crust is approximated
 133 by a smooth anisotropic layer to account for the crustal effects on wave propagation and
 134 dispersion. GLAD-M25 inverts for the bulk sound speed and vertically and horizontally
 135 polarized V_S in the mantle above 660 km. Its starting model is S362ANI (Kustowski et
 136 al., 2008) for the mantle and Crust2.0 (Bassin et al., 2000) for the crust. As in the start-
 137 ing model S362ANI, GLAD-M25 uses a parameterization that includes first- and second-
 138 order discontinuities in the radial direction, permitting abrupt changes in the pattern
 139 of heterogeneity across the mantle transition zone (MTZ). Both of the global tomographic
 140 models resolve broad plumes rising from the CMB to the upper mantle beneath many
 141 hotspots (French & Romanowicz, 2015; Lei et al., 2020). These enforced vertical discon-
 142 tinuities in GLAD-M25 could introduce artifacts to the resolved plume shapes around
 143 the MTZ, but plume structures resolved in the lower mantle should remain robust, dis-
 144 cussed later.

145 We define plume conduits based on three considerations. *First*, we require plume
 146 conduits to be continuous pathways from the lithosphere to the CMB. *Second*, we require
 147 that plume conduits be slower than average across all mantle depths (i.e., having a neg-
 148 ative δV_S). *Third*, we seek plume conduits for which the temperature anomaly implied
 149 by wave speed variations is consistent with petrological constraints on plume excess tem-
 150 perature. The third criterion may not always be satisfiable due to limitations in tomo-
 151 graphic modeling, discussed later.

152 Following our criteria, we manually traced the conduits of 20 plumes (listed in Ta-
 153 ble S1), of which the buoyancy flux is larger than 1000 kg/s (Jackson et al., 2021) and
 154 are well-resolved in both SEMUCB-WM1 and GLAD-M25. We exclude the Yellowstone
 155 plume as it is only well-resolved in GLAD-M25. We include the Canary and St. Helena
 156 plumes, of which the buoyancy flux is only 800 and 500 kg/s, respectively, because sim-
 157 ilar plume shapes are clearly resolved in both tomographic models. Moreover, the OIBs
 158 associated with both hotspots display isotopic signatures supporting a deep mantle ori-
 159 gin.

160 The plume conduits are traced in a headset-based immersive 3D visualization en-
 161 vironment. We use the Valve Index VR headset and controllers and the Paraview 5.10.0
 162 (Ahrens et al., 2005) visualization software. The identification of plume conduits was car-
 163 ried out using the following steps:

- 164 1. The traced conduit (TC) of each plume can be divided into an upper-mantle, a
 165 mid-mantle, and a lower-mantle part. We first identify candidate conduits (CCs)
 166 - conduit-like vertical negative δV_S structures - that extend vertically across the
 167 mid mantle near each surface hotspot. There may be multiple candidate conduits
 168 for each hotspot, and we seek conduits that are closer to the hotspot's surface ex-
 169 pression.
- 170 2. We use pipelines (control points connected by line segments) to represent the path-
 171 way of the traced conduit, where the control points are assigned every 200 km from
 172 250 to 2450 km depth. We seek an upper-mantle TC, which connects the surface
 173 hotspot with the upper-end of the mid-mantle TC, and a lower-mantle TC, which
 174 starts from the lower-end of the mid-mantle TC. Where there is ambiguity, we pre-
 175 fer more vertical plume conduits.
- 176 3. After tracing the plume conduits, we validate our TCs according to two criteria.
 177 First, the δV_S along a TC should not be positive. Second, we use the plume and
 178 ambient mantle potential temperature calculated from olivine-liquid equilibria (Putirka,
 179 2008) to estimate the excess temperature of plumes. We then calculate the pro-
 180 file of $d(\ln V_S)/dT$ (Figure S1) assuming that the plume has a pyrolytic compo-
 181 sition and use the profile of $d(\ln V_S)/dT$ to calculate δV_S corresponding to the petrologically-
 182 estimated excess temperature at all depths for each plume that has an estimation.
 183 δV_S along the TC should be comparable to δV_S converted from the petrologically-
 184 estimated excess temperature at some depths above 1250 km. The second crite-
 185 rion is not hardwired because the variable resolution, parameterization, and reg-
 186 ularization of global tomographic models can all contribute to modeled V_S vari-
 187 ations.

188 3 Results

189 We describe the general properties of the traced plume conduits (Figure 2), start-
 190 ing from describing the slowness of the traced conduits. We then describe overall trends
 191 in the amount of offset from the surface location, the tilt (measured in degrees away from
 192 the vertical) of plume conduits, and the depths at which large offsets or tilts occur. We
 193 describe the shapes of individual plume conduits in greater detail later.

194 3.1 Slowness along plume conduits

195 The δV_S along conduits traced from SEMUCB-WM1 and GLAD-M25 is generally
 196 between 0% and -2%, comparable with each other (Figure 3-4). We find that plumes ori-
 197 ginating from the African LLSVP are faster than plumes stemming from the Pacific LLSVP
 198 above ~ 1250 km depth in SEMUCB-WM1 and at all depths in GLAD-M25 (Figure 5b,
 199 c, g, h). We also evaluate the average δV_S of conduits traced from SEMUCB-WM1 in
 200 GLAD-M25 as well as conduits traced from GLAD-M25 in SEMUCB-WM1 (Figure 5d,
 201 e, i, j). When plumes traced in one tomographic model are evaluated in the other to-
 202 mographic model, the average δV_S along TCs around the Pacific LLSVP remains nega-
 203 tive at all depths, while it is negative only in the lower mantle for TCs around the African
 204 LLSVP.

205 3.2 Observed morphology

206 Tilt angles along the traced conduits generally remain smaller in the lower man-
 207 tle (usually $< 60^\circ$) than in the upper mantle with a few exceptions (Figure 6). For ex-
 208 ample, the Louisville and Azores plumes have a tilt angle ($60 - 70^\circ$) below 2000 km in
 209 SEMUCB-WM1. A comparison of the tilt angles of plumes (Figure 6) and the offsets
 210 of plume conduits (azimuth and distance, shown in Figure 7) shows that large tilt an-
 211 gles are associated with abrupt changes in offset distances and/or azimuths of TCs. Changes
 212 in offset azimuths and distances are small where the tilt is closer to vertical. The azimuth

213 of a conduit is measured by assuming its hotspot as the origin, 0 degree at the north,
 214 and counting clock-wise. Due to the manual process of conduit tracing, the uncertainty
 215 in tilt of TCs is at least 5° . Hence TCs with tilt less than this should be interpreted as
 216 nearly vertical. We do not report the average tilt angle of each conduit because these
 217 values do not accurately describe the shape of conduits. For example, in SEMUCB-WM1,
 218 the TC of Samoa has a similar average tilt angle (16.9°) to the TC of Pitcairn (16.1°).
 219 However, the TC of Samoa appears to be ponded and deflected at 660 and 410 km depth,
 220 while the TC of Pitcairn tilts gently across the whole mantle.

221 Plume conduits traced in SEMUCB-WM1 and GLAD-M25 usually root at loca-
 222 tions offset from their surface hotspots by $5 - 10^\circ$ and most of the offset occurs in the
 223 upper mantle. A few plume conduits show larger offsets. The TCs of Galapagos, San Fe-
 224 lix, and Tahiti root at locations offset from their surface hotspots by more than 10° in
 225 both tomographic models (Figure 2 and 7). The offsets of conduits traced from SEMUCB-
 226 WM1 in the upper mantle can easily exceed 5 degrees (Figure 7), which converts to $>$
 227 500 km offsets, while those of conduits traced from GLAD-M25 appear to be much smaller.

228 **3.2.1 Paired plumes**

229 In SEMUCB-WM1, the MacDonal and Pitcairn plumes seem to branch from the
 230 same conduit in the lower mantle and the Macdonald plume is significantly deflected at
 231 ~ 1250 km depth (Figure 8a). The Canary and Cape Verde plumes also appear to share
 232 the same conduit from the CMB to at least ~ 1250 km depth and branch into two con-
 233 duits separated by $\sim 15^\circ$ in the upper mantle (Figure 8b).

234 In GLAD-M25, we identify CC with a similar shape as what is observed in SEMUCB-
 235 WM1 below the Canary and Cape Verde hotspots. We interpret Canary and Cape Verde
 236 as two adjacent plumes rising parallel to each other though this CC could be interpreted
 237 as either two separate conduits or one broad plume branching into two secondary plumes
 238 as it crosses the 660 km discontinuity. CCs of the Pitcairn and Macdonald plumes look
 239 less like those in SEMUCB-WM1. These two plumes seem to emerge from different loca-
 240 tions at the CMB and merge into a broad plume conduit between 660 and 2000 km
 241 depth and branch again above 660 km depth.

242 The San Felix and Juan Fernandez plumes are another potential paired plumes.
 243 These two plumes generally share the same CC in the mid-mantle in both tomographic
 244 models (Figure S2). We interpret it as two adjacent plumes rising parallel to each other
 245 and trace their conduits based on this interpretation. The conduit of San Felix is not
 246 resolved between 1250 and 660 km in SEMUCB-WM1 and above 660 km in GLAD-M25.
 247 The conduit of Juan Fernandez is generally well resolved at all depths in both tomographic
 248 models.

249 **3.2.2 Iceland**

250 The Iceland plume is generally vertical in both tomographic models, but the de-
 251 tailed shape of the plume is different. Starting from the surface hotspot, the traced con-
 252 duit from SEMUCB-WM1 is offset towards the northeast above ~ 350 km and then off-
 253 set back towards the hotspot at ~ 660 km. The conduit remains generally vertical be-
 254 low 660 km and slightly tilts towards the east below ~ 2000 km (Figure 6,7, and 8c).
 255 Its TC from GLAD-M25 is vertical above 660 km, tilts first towards the east between
 256 660 and 1000 km depth then towards the west between ~ 1250 and 1500 km depth, and
 257 remains vertical below 1500 km.

258

3.2.3 Hawaii

259

260

261

262

263

264

The Hawaii plume appears to be mostly vertical in SEMUCB-WM1, while it appears to largely tilt towards the southeast in GLAD-M25. Its conduit is well resolved in SEMUCB-WM1 but not well resolved between 410 and 660 km depth in GLAD-M25 (Figure 8d). Although the TCs from SEMUCB-WM1 and GLAD-M25 are not consistent, both tomographic models resolve a similar CC between 660 and 1250 km depth below the surface hotspot location and a similar CC location at the CMB (Figure 8d).

265

3.2.4 Samoa, St Helena, Reunion, and Caroline

266

267

268

269

270

271

272

273

Similar CCs are identified in both tomographic models for the Samoa, St Helena, Reunion, and Caroline plumes. These plumes remain nearly vertical or slightly tilt in the lower mantle and tilt more heavily in the upper mantle (Figure 9a-c). We noticed that amplitudes of negative δV_S along these TCs from SEMUCB-WM1 vary smoothly and reach a maximum near 660 km. Amplitudes of the negative δV_S along these TCs from GLAD-M25, however, decrease abruptly above the 660 km discontinuity. These negative δV_S amplitudes are larger (slower) than those of conduits traced from SEMUCB-WM1 by 0.5-1.0 % δV_S below ~ 2000 km (Figure 3 and 4).

274

3.2.5 Azores, Easter, Galapagos, Kerguelen, Marquesas, and Tahiti

275

276

277

278

279

280

We notice that for the Azores, Easter, Galapagos, Kerguelen, Marquesas, and Tahiti plumes, similar CCs are resolved in the two tomographic models but different TCs are identified (Figure 9d and S3-5). One of the main causes is the poor inter-model agreement above 660 km and below 2000 km. The other main cause is that the δV_S of CCs with similar shapes can amplify at different depths in different tomographic models. It can result in very different interpretations of the most-reasonable conduit path.

281

4 Discussion

282

283

284

285

286

287

We first demonstrate the reliability of our traced conduits to justify that our TCs represent seismically slow paths through the mantle. We then compare our TCs with modeled conduits and discuss the reasons for their differences. Next, we discuss the implications for mantle and plume dynamics from our observed plume shapes and slowness along conduits. We conclude our discussion by proposing some applications of our TCs in future studies of plume dynamics.

288

4.1 Reliability of traced conduits

289

290

291

292

293

294

295

296

297

298

299

300

301

302

303

Seismic tomography is a mixed-determined inverse problem, and there exist many possible Earth structures that are equally compatible with seismic observables. The shapes of plumes could vary between different regional and global tomographic models due to different parameterization/regularization choices and different earthquake events used to constrain the tomographic models (French & Romanowicz, 2015; Wamba et al., 2021, 2023). Hence, one might question the veracity of mantle plume shapes determined on the basis of seismic tomography. Several lines of evidence suggest that the imaged and traced plume conduits are likely representative of real mantle structures. *First*, the slow V_S structures near many hotspots are similar between the two models, suggesting that the imaged features are robust. *Second*, the average slowness along TCs is much greater than the average slowness along modeled or vertical conduits (Figure 5a-c, f-h). To further assess the robustness of the traced plume conduits, we evaluate the slowness along Pacific TCs obtained from SEMUCB-WM1 and GLAD-M25 in other P- and S- velocity tomographic models. We find that our Pacific TCs traced from GLAD-M25 are slower than the MCs and vertical conduits (VCs) in the lower mantle (below ~ 660 – 1000 km

depth) when they are evaluated in most of the other models (Figure 5i and S2 g-k). Our Pacific TCs traced from SEMUCB-WM1 are slower than the MCs and vertical conduits (VCs) but in a more restricted depth range between ~ 1250 and 2100 km depth (Figure 5d and S2 a-d). (See Text S2 in the Supporting Information for more details.) This suggests that both sets of traced conduits, especially TCs from GLAD-M25, are more compatible with many other tomographic models than the modeled and vertical conduits in the mid to lower mantle.

4.2 Comparison between traced and modeled conduits

Simplified numerical models of mantle plume shapes have been used widely in geodynamics to understand the mobility of deep mantle hotspots and to establish the moving hotspot reference frames necessary for absolute plate reconstructions (e.g., Matthews et al., 2016). We compare modeled conduits (MCs) from (Steinberger & Antretter, 2006) with our traced conduits. These numerical models of plume dynamics start with a mantle buoyancy structure based on a tomographic model filtered to long wavelength. The buoyancy structure is reconstructed backwards in time through the reversal of buoyancy forces and the application of time-reversed plate reconstructions at the surface while ignoring the effects of thermal diffusion, which cannot be time-reversed due to non-uniqueness. This yields a model of *long-wavelength* (much longer wavelength than the widths of plumes) mantle flow in space and time. Then, initially vertical plume conduits are advected by the flow field forward in time. Previous studies demonstrated that the shapes of MCs are not very sensitive to the tomographic model used to compute the mantle flow field, the details of the plate reconstructions used, or the detailed mantle viscosity structure (Steinberger & O’Connell, 1998; Steinberger, 2000; Steinberger & Antretter, 2006; Williams et al., 2019).

The tilt angles and offsets of MCs show that most of MCs slightly tilt (tilt angle $< 30^\circ$) below 660 km. This is likely because the deformation rate is slow due to the high viscosity of the lower mantle. Larger tilt angles (up to $> 90^\circ$) of MCs observed above 660 km (Figure 6) are mainly due to the oscillations of the tightly spacing conduit elements in the lower-viscosity upper mantle. The offsets of modeled conduits (shown in Figure 7) show that MCs in fact tilt gently at these depths. Our TCs suggest that plumes generally slightly tilt in the lower mantle, but large tilt angles in the mid-mantle below 660 km are observed for many TCs from both tomographic models (e.g., Macdonald, Samoa, St Helena, and Tristan) (Figure 6). TCs generally have more complex shapes than MCs, especially in the mid-mantle.

Although the paths of TCs and MCs are generally not in very good agreement (Figure 2, Table S1), there are a couple of exceptions. TCs of plumes located at the edge of LLSVPs (Canary, Juan Fernandez, San Felix, St Helena, and Reunion)(Figure 7) seem to agree with their MCs better than TCs of plumes located near the center of LLSVPs. TCs of these plumes share similar offset directions with their MCs, while the MCs have $5 - 10^\circ$ more total offset distances than the TCs. These plumes have relatively simple plume shapes, that is, the offset direction of a TC does not change with depth. TCs of plumes located around the center of LLSVPs are usually vertical in the lower mantle but meander in the middle and upper mantle. Because of the physics included in the models, all MCs only have simple plume shapes (without stagnation or meandering). They are always smooth curves extending from the LLSVPs to the surface hotspots. We discuss this difference more in the next section.

The average seismic velocities of the TCs, MCs, and VCs are slower than the ambient mantle at all depths. However, TCs from SEMUCB-WM1 are up to 6 times slower than MCs and 3.7 times slower than VCs in the upper mantle, while they are 1.2-3 times slower than MCs and VCs in the lower mantle. TCs from GLAD-M25 are 1.1-3 times slower than MCs and VCs across the mantle. The average velocities of MCs are slower

355 than the those along VCs only in the lower mantle (Figure 5a, f), which is consistent with
 356 the analysis of MCs and VCs done using older tomographic models (Boschi et al., 2007).
 357 The δV_S along MCs is often close to 0% or even positive in the upper mantle (Figure 3
 358 and 4), while the δV_S along TCs is negative in most cases. There are a few exceptions
 359 in SEMUCB-WM1 (Cape Verde and San Felix) and GLAD-M25 (Azores, Canary, Hawaii,
 360 San Felix, Tahiti, and Tristan). In these cases, no CC can be identified at some depths
 361 in the upper mantle. This may indicate that the global tomographic model does not re-
 362 solve the plume conduit at these depths. It is expected that plume radius can significantly
 363 decrease as a plume rising from the more viscous lower mantle to the less viscous upper
 364 mantle (Leng & Gurnis, 2012).

365 4.3 Implications of the slowness along plume conduits

366 The excess temperature of a purely thermal plume conduit is not expected to change
 367 significantly with depth since plumes rise rapidly relative to the thermal diffusion timescale
 368 and mantle heat production is negligible on the timescale of material ascent through a
 369 plume conduit. For example, the exothermic phase transition (olivine to wadsleyite) at
 370 410 km depth, and shear heating may be able to increase the temperature of a plume,
 371 but they are secondary effects compared with the plume’s inherent excess temperature.
 372 This implies that if a mantle plume is purely thermal, the amplitude of its δV_S should
 373 generally vary following the thermodynamically determined $d(\ln V_S)/dT$ profile with depth.
 374 Our observations from both tomographic models, however, show that the variation of
 375 δV_S along plume conduits almost never strictly follow the $d(\ln V_S)/dT$ profile, which sug-
 376 gests that non-thermal variations are present in plume conduits.

377 Non-thermal variations in mantle plumes include differences in intrinsic composi-
 378 tion, water content, grain size, and melt fraction. At the 410 km discontinuity, the phase
 379 transition from wadsleyite to olivine may result in water release when plume materials
 380 rise and cross this boundary because wadsleyite has a higher water-bearing ability than
 381 olivine (W. Wang et al., 2019). Increasing water content can reduce V_S (C. Liu et al.,
 382 2023) and may cause partial melting in this region, further reducing V_S (Chantel et al.,
 383 2016). Isotopic measurements of OIBs and numerical models suggest that LLSVPs may
 384 be composed of a variety of different materials, ranging from primordial materials that
 385 get preserved at the CMB since the differentiation in early Earth’s evolution (Labrosse
 386 et al., 2007; Deschamps et al., 2012) to piles of recycled oceanic crusts (Olson & Kin-
 387 caid, 1991; Brandenburg & van Keken, 2007). For many of the traced conduits, we find
 388 that δV_S in the lowermost mantle is slower than expected on the basis of $d(\ln V_S)/dT$.
 389 The incorporation of compositionally-distinct material within the lowermost mantle is
 390 one possible explanation for the slower than expected velocities (Figure 3 and 4).

391 The systematically faster plumes (in the upper- and mid-mantle) originating from
 392 the African LLSVP than those originating from the Pacific LLSVP (Figure 5b, c, g, h)
 393 are consistent with previous estimates of plume excess temperature based on upper man-
 394 tle wavespeed variations (Bao et al., 2022). Y. Wang and Wen (2007) and He and Wen
 395 (2009) also show that the two LLSVPs have different shape and topology. They may in-
 396 dicate that the two LLSVPs have different origins, but we cannot rule out the possibil-
 397 ity that the faster plumes from the African LLSVP are caused by different seismic data
 398 coverage between the Pacific and the Atlantic regions.

399 4.4 Implications of diverse plume shapes

400 The shape of a plume conduit depends on both the plume’s properties and its in-
 401 teraction with its surrounding mantle. Buoyancy, which is determined by $\Delta\rho$, the dif-
 402 ference between the effective density of a plume and the density of its surrounding man-
 403 tle ($\Delta\rho = \rho_{plume} - \rho_{mantle}$), controls the behaviours of a plume as it rises. The buoy-
 404 ant ascent of plume material and its interaction with the large-scale mantle flow will re-

405 sult in different plume conduit shapes. The composition of the plume, the pressure in-
 406 duced phase transitions, and the excess temperature (temperature difference between
 407 the potential temperature of a plume and the ambient mantle) together determine $\Delta\rho$.
 408 When a plume has a positive buoyancy ($\Delta\rho < 0$), it will rise, and it will start sinking
 409 when it has a negative buoyancy. When $\Delta\rho$ is close to or slightly smaller than 0, a plume
 410 could be ponded or develop a variety of complex shapes (Kumagai et al., 2008; Xiang
 411 et al., 2021).

412 The mantle viscosity structure and flow patterns of the ambient mantle also affect
 413 plume shapes. The mobility of a plume, that is how easily it gets deformed, is expected
 414 to be smaller in a more viscous than in a less viscous region (H. Liu & Leng, 2020). Large-
 415 scale mantle flows driven by thermal convection, surface plate motion, and subduction
 416 could shear plume conduits or largely deflect the secondary plume stemming from a pond-
 417 ing primary plume (Steinberger, 2000; Farnetani & Samuel, 2005).

418 The more complex shapes of our TCs than the MCs suggest that the mantle con-
 419 vection models used to determine MCs may not consider all major factors affecting plume
 420 shapes, especially in the mid-mantle across and below the MTZ, where plume ponding
 421 and large tilt angles are only observed in TCs.

422 First, the mid-mantle below the MTZ could have significant viscosity variations (Marquardt
 423 & Miyagi, 2015; Rudolph et al., 2015; Shim et al., 2017), which indicates a more com-
 424 plex rheology than the numerical models' assumption that only a few deformations oc-
 425 cur and diffusion creep is predominant at these depths (Ferreira et al., 2019). Further-
 426 more, the transition from ringwoodite to bridgmanite at 660 km, which can lead to plume
 427 ponding at this depth, is not considered neither. In return, the numerical models lack
 428 the ability to produce plumes that are ponded and deflected at different depths due to
 429 their simplified physics, which does not consider the composition variations, phase tran-
 430 sitions, nor a temperature-dependent or strain-rate-dependent viscosity.

431 Second, the mantle flow field converted from the global tomographic model (Steinberger
 432 & O'Connell, 1998) may not be accurate at a smaller scale due to our current incom-
 433 plete understanding of mantle dynamics. MCs are determined based on the assumption
 434 that a plume rose to the surface vertically within a short time and left a vertical 100-
 435 kilometer-radius conduit that gets passively advected by the large-scale mantle flows later.
 436 However, this assumption is only valid if mantle plumes are purely thermal. Recent seis-
 437 mic tomographic models have imaged plume conduits with a radius of ~ 500 km (French
 438 & Romanowicz, 2015) and much more complex morphology (Tsekhmistrenko et al., 2021;
 439 Celli et al., 2021; Wamba et al., 2023). Such broad plumes may not only be passively
 440 advected, but also influence the mantle flow field. Plumes with such large radius would
 441 have buoyancy fluxes that are much higher than previous estimations (Sleep, 1990; King
 442 & Adam, 2014). Together with the complex plume shapes, they suggest that many, if
 443 not all, mantle plumes are thermochemical rather than purely thermal. For example, a
 444 plume that incorporates an eclogitic component has a lower buoyancy flux and a larger
 445 radius than a purely thermal plume, which is more consistent with observations (Dannberg
 446 & Sobolev, 2015).

447 At ~ 410 km depth, previous numerical models suggest that plumes with some eclogitic
 448 component will have a buoyancy barrier due to the different phase transitions that oc-
 449 cur in pyrolitic and eclogitic materials. This buoyancy barrier can result in plume pond-
 450 ing and the emergence of a secondary plume (Farnetani & Samuel, 2005; Dannberg &
 451 Sobolev, 2015). It can potentially explain the ponding of Samoa, a large tilt angle, and
 452 a large change in offset distance observed in SEMUCB-WM1 at this depth (Figure 6,9a).

453 Large tilt angles at 660 km depth mostly reflect plume ponding, which could be
 454 caused by the combined effect of the ~ 30 -fold viscosity increase from above to below
 455 660 km suggested by many geophysical studies (Hager, 1984; Mitrovica & Forte, 1997)

as well as the endothermic phase transition from ringwoodite to bridgmanite (Faccenda & Dal Zilio, 2017). The phase transition can cause plume ponding as the hotter plume materials undergo this phase transition at a shallower depth, hindering ascent. Several scenarios may happen after a primary plume is ponded at this depth. First, the primary plume could penetrate the 660-discontinuity broadly while some plume materials are ponded. These ponding materials become so hot that there is a significant viscosity reduction, allowing the conduit to be laterally deflected by hundreds of kilometers (Tosi & Yuen, 2011). This scenario is observed for St. Helena and Tristan in both tomographic models (Figure 6, 7, 9b and S6).

When the primary plume cannot penetrate the 660-discontinuity in the first place, significant amount of plume materials will accumulate at this depth. The ponding materials will spread like a pancake and secondary plumes can develop from anywhere above the ponding zone. As a result, the offset distance between an upper-mantle secondary plume and a lower-mantle primary plume is not large, while the offset azimuth can be irrelevant to the flow patterns (Caroline in GLAD-M25, Azores, Iceland, Reunion in both tomographic models) (Figure 6, 7, 8c, 9c, S3 c and d). They may resemble the “plume-tree” model proposed in Liu and Leng (2020), which requires a thin low-viscosity layer beneath the 660 km ponding depth and a low-viscosity upper mantle to allow secondary plume(s) develop from any part of the ponding materials.

At a greater depth ~ 1250 km, large tilt angles observed of Tahiti in both tomographic models, Hawaii in GLAD-M25, and Kerguelen in SEMUCB-WM1 (Figure 6) could arise if the viscosity is higher around this depth than in the mantle above and below it. Owing to the higher viscosity, conduits tilt less around this depth, so the conduit above this depth could be preferentially deflected by mantle flow. Some inversions of geophysical data suggest that there exists a viscosity hump, a one-to-two-order of magnitude viscosity increase, between 800 and 1200 km depth (King & Masters, 1992; Mitrovica & Forte, 1997; Rudolph et al., 2015). Studies on mineral physics also suggest that the increasing strength of ferropericlase (Marquardt & Miyagi, 2015; Deng & Lee, 2017) and decreasing the iron-enrichment in bridgmanite (Shim et al., 2017) at the mid-mantle depth can both result in this mid-mantle viscosity hump.

Another mechanism that may produce large tilt angles at ~ 1000 – 1250 km (Canary and MacDonald in SEMUCB-WM1) is plume ponding and secondary plumes emerging. This mechanism is proposed by Wamba et al. (2023) to explain alternating vertical conduits and horizontal ponding zone observed for the Reunion and Comores plumes from ~ 1000 km depth to the top of the asthenosphere in the latest tomographic models. There is no known endothermic phase transition, which could cause plume ponding, at these depths. However, a denser mantle below ~ 1000 km depth due to its higher basalt content (Ballmer et al., 2015) could cause plume ponding at this depth if the thermal expansion effect is not strong enough to reduce the plume effective density to be smaller than the mantle density above ~ 1000 km (Xiang et al., 2021). Seismic observations imply a not-global discontinuity presenting at 1000 km depth (Zhang et al., 2023), which may indicate a compositional layered mantle.

Other than these various behaviours of a single plume conduit, plume merging may further complicate the observed plume shapes. For example, we identify two CCs for Galapagos in the mid-mantle that merge into one CC with $< 1\%$ δV_S above 660 km in SEMUCB-WM1. It may represent that two adjacent conduits are ponded at 660 km and the ponding zones of them merge into one conduit or these two resolved CCs are caused by a lack of resolution in SEMUCB-WM1 as they are only observed in SEMUCB-WM1. The TCs of Macdonald and Pitcairn from GLAD-M25 suggest these two plumes merge in the mid-mantle and branch above 660 km. Merging of two adjacent plumes has been demonstrated by both lab experiment (Moses et al., 1991) and numerical models (e.g., Lewis-Merrill et al., 2022; Brunet & Yuen, 2000), and the branching of the merged conduit could be explained by secondary plumes emerging from a ponding plume.

509 Given all these uncertainties in our interpretations of plume dynamics from observed
 510 plume shapes, our TCs are useful for future numerical modeling. For example, idealized
 511 plume models can explore under which geodynamics setting, the observed plume shapes
 512 can be reproduced. Our TCs can also provide a better schematic model for future stud-
 513 ies to interpret the geochemical heterogeneity of OIBs from different hotspots. For ex-
 514 ample, previous studies have tried to interpret the heterogeneous isotopic signals of OIBs
 515 from neighbouring hotspots by correlating them with the vertical projection of the hotspots
 516 onto the CMB (Huang et al., 2011; Harpp & Weis, 2020) or interpreting these isotopic
 517 signals under simplified schematic plume models (Williams et al., 2019; Cordier et al.,
 518 2021). Our TCs can provide information about potential inter-plume interactions and
 519 the ascent history of plumes, which can be critical to the interpretation of geochemical
 520 observations.

521 5 Conclusion

522 Broad plumes clustering around LLSVPs have been recognized from the latest global
 523 tomographic models. Our study presents a systematic analysis of the pathways of these
 524 plume conduits. We carried out an analysis of the shapes of plume conduits in an im-
 525 mersive headset-based virtual reality (VR) environment. The wavespeed variations along
 526 the traced conduits from SEMUCB-WM1 and GLAD-M25 generally appear to be slower
 527 than the conduits predicted by geodynamic models and vertical conduits in the mid to
 528 lower mantle depth regardless of which tomographic models they are evaluated in. The
 529 traced conduits are 1.1 – 3 times slower than either modeled or vertical conduits. This
 530 suggests that our manually-traced conduits are more consistent with the locus of slow
 531 seismic velocities within the mantle than either the vertical conduits that some authors
 532 have assumed when relating surface observables to deep mantle structures or the shapes
 533 of plume conduits predicted using physically simplified geodynamic models. Moreover,
 534 our traced conduits are more consistent with the petrologically-determined excess tem-
 535 perature than either of the other types of conduits.

536 In our manually traced conduits, the total amount of offset from the surface to the
 537 deep mantle is comparable between many traced and modeled conduits (usually smaller
 538 than 10°), while the offset direction of traced and modeled conduits usually differ. Some
 539 traced conduits of plumes stemming from the edge of the LLSVPs (Canary, Juan Fer-
 540 nando, Reunion, San Felix, and St Helena) tend to be $5 - 10^\circ$ less offset than their mod-
 541 eled conduits, but the traced and modeled conduits share similar offset directions. Our
 542 traced conduits reveal a tendency for plumes to stagnate or to be offset at mid-mantle
 543 depths (660 – 1250 km), a behavior that is not captured in modeled conduits. Previous
 544 geophysical studies, mineral physics studies, and geodynamics modeling provide multi-
 545 ple mechanisms that could contribute to plume ponding or deflection, including the buoy-
 546 ancy barrier induced by phase transitions and the viscous decoupling of conduits. The
 547 large variations of V_S anomaly along plume conduits and the complex observed plume
 548 shapes together suggest that many plumes are thermochemical. Our analysis of plume
 549 conduit shapes provides a dataset that can be of value across multiple disciplines includ-
 550 ing geodynamic modeling, geochemistry, and mineral physics.

551 6 Figures

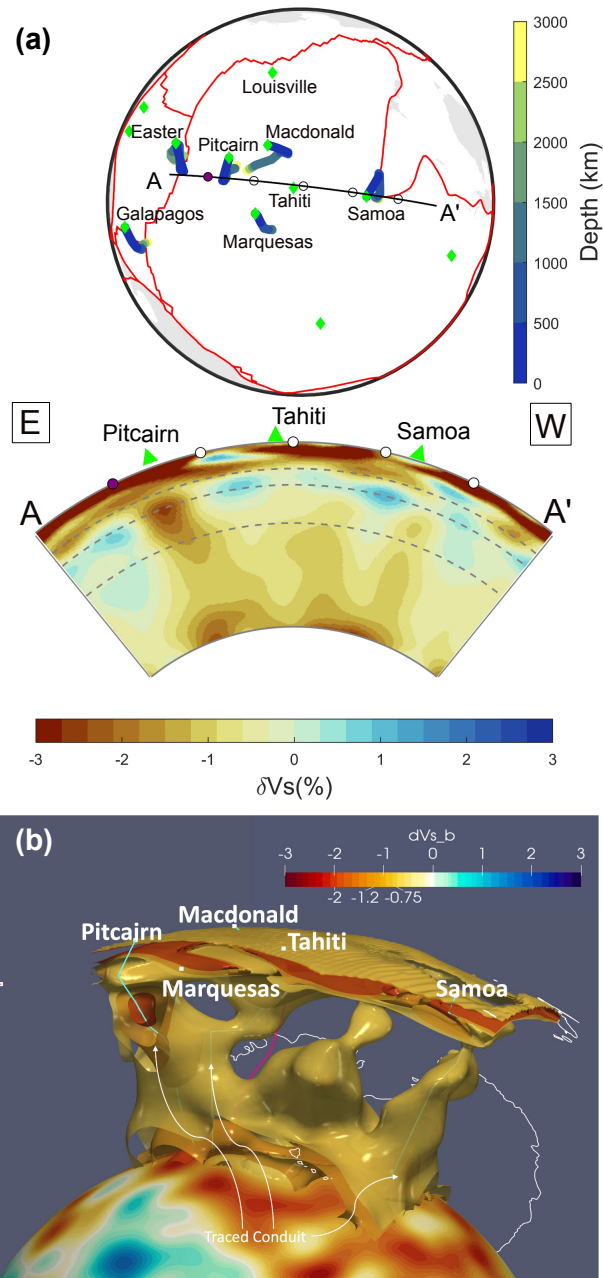


Figure 1. (a) Cross section of Pacific plumes in SEMUCB-WM1 and the location of the cross-section on the map, and (b) the 3D image of -2%, -1.2%, and -0.75% δV_S isosurfaces taken from the same region.

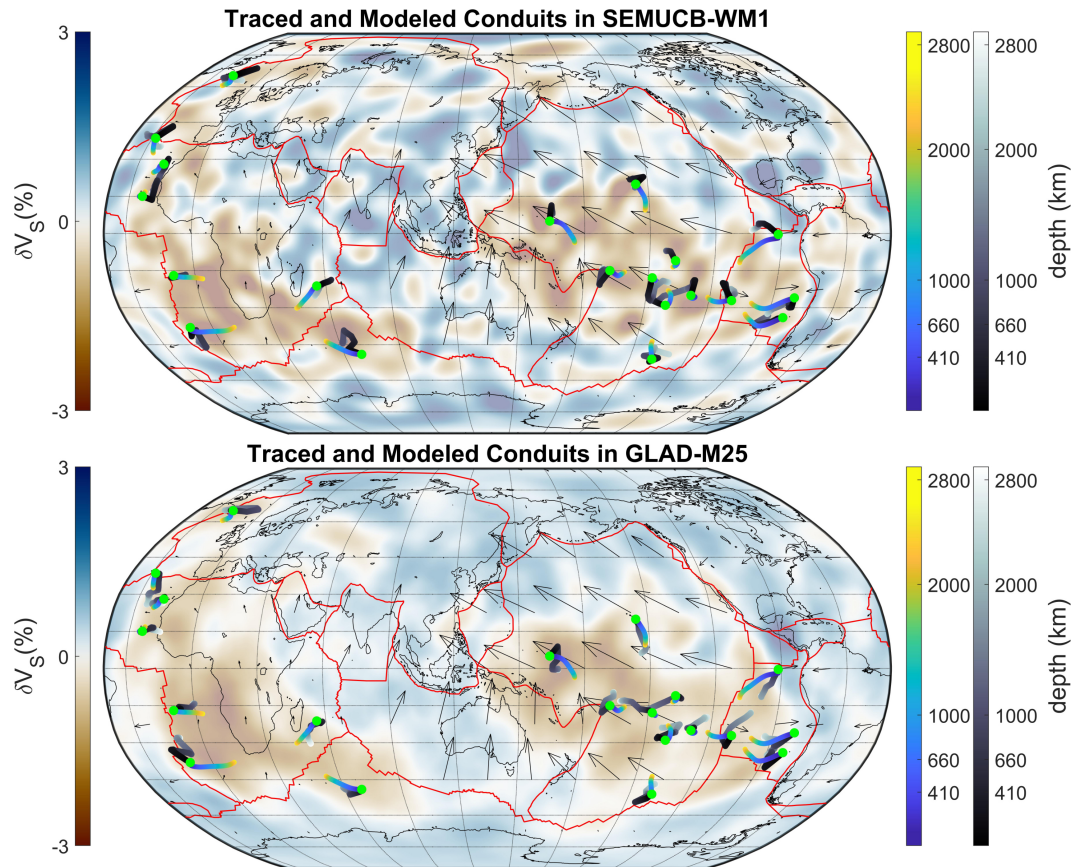


Figure 2. Traced and modeled (Steinberger & Antretter, 2006) plume conduits in SEMUCB-WM1 (top) and in GLAD-M25 (bottom). The colorful dots represent modeled conduits, while black-white dots represent traced conduits. The green circles represent the location of hotspots. The background shows δV_S at 2850 km depth. Plate motions in the spreading-aligned mantle reference frame of Becker et al. (2015) are shown with gray arrows.

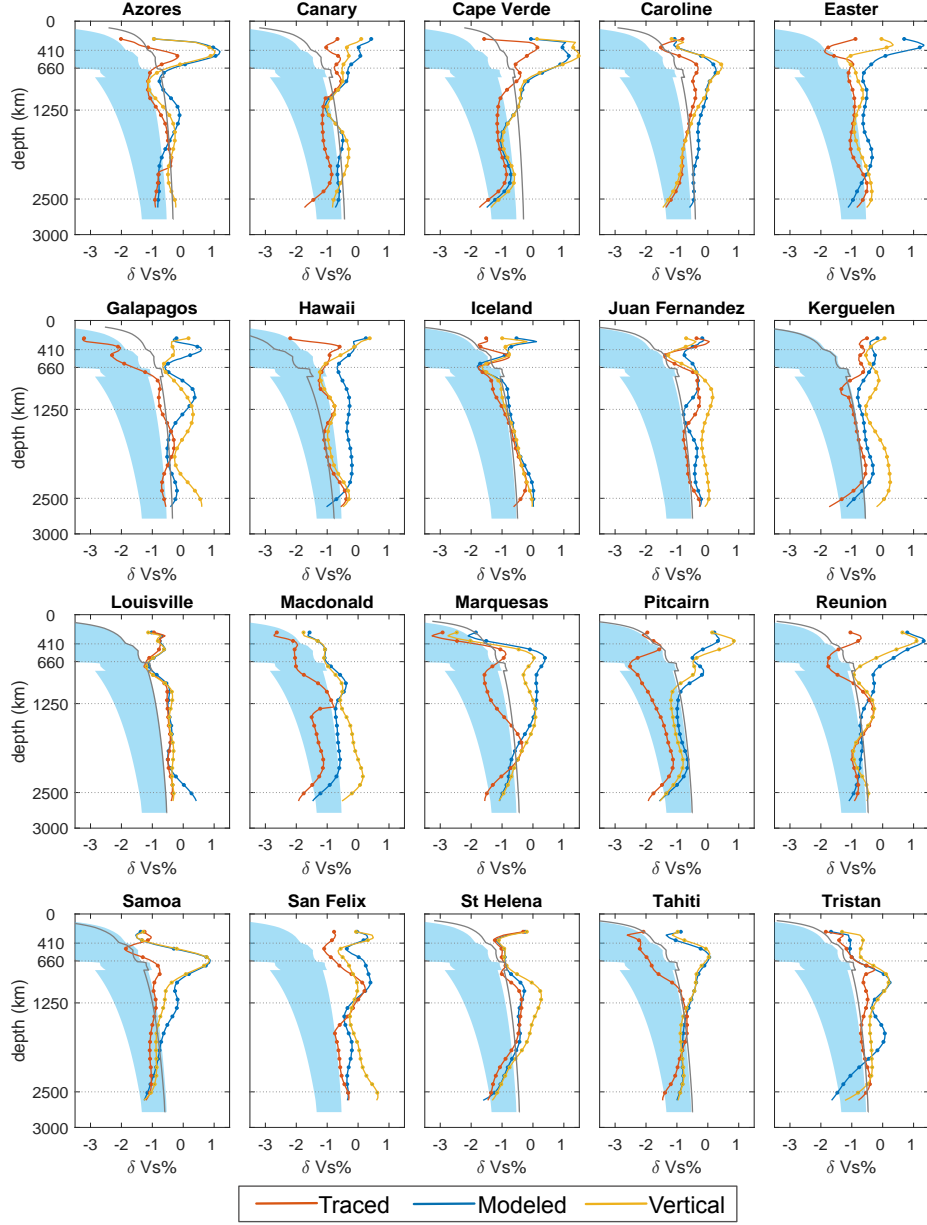


Figure 3. The depth profile of δV_S along 20 plume conduits in SEMUCB-WM1. Red represents the traced conduits. Blue represents the conduits modeled in Steinberger and Antretter (2006). Yellow represents the vertical conduits. The gray solid line is the corresponding δV_S of the petrologically estimated excess temperature from Putirka, 2008. The blue shade is the reference profile for expecting δV_S along a conduit given excess temperatures between 200 and 500 K calculated from the $d(\ln V_S)/dT$ profile (Figure. S1). The tomographically-resolved slowness along plume conduits can likely be interpreted as a lower bound on the true slowness.

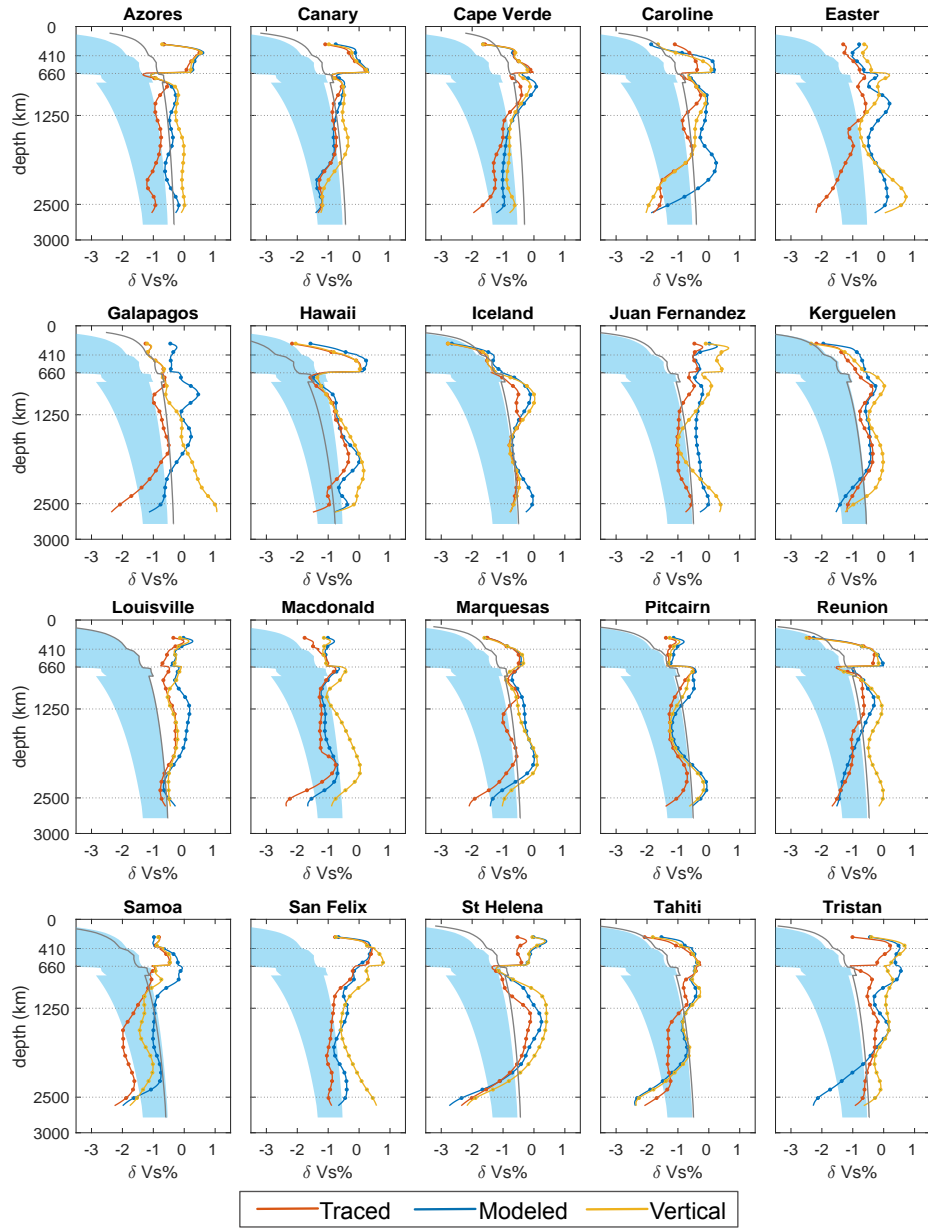


Figure 4. The depth profile of δV_S along 20 plume conduits in GLAD-M25 similar to Figure 3.

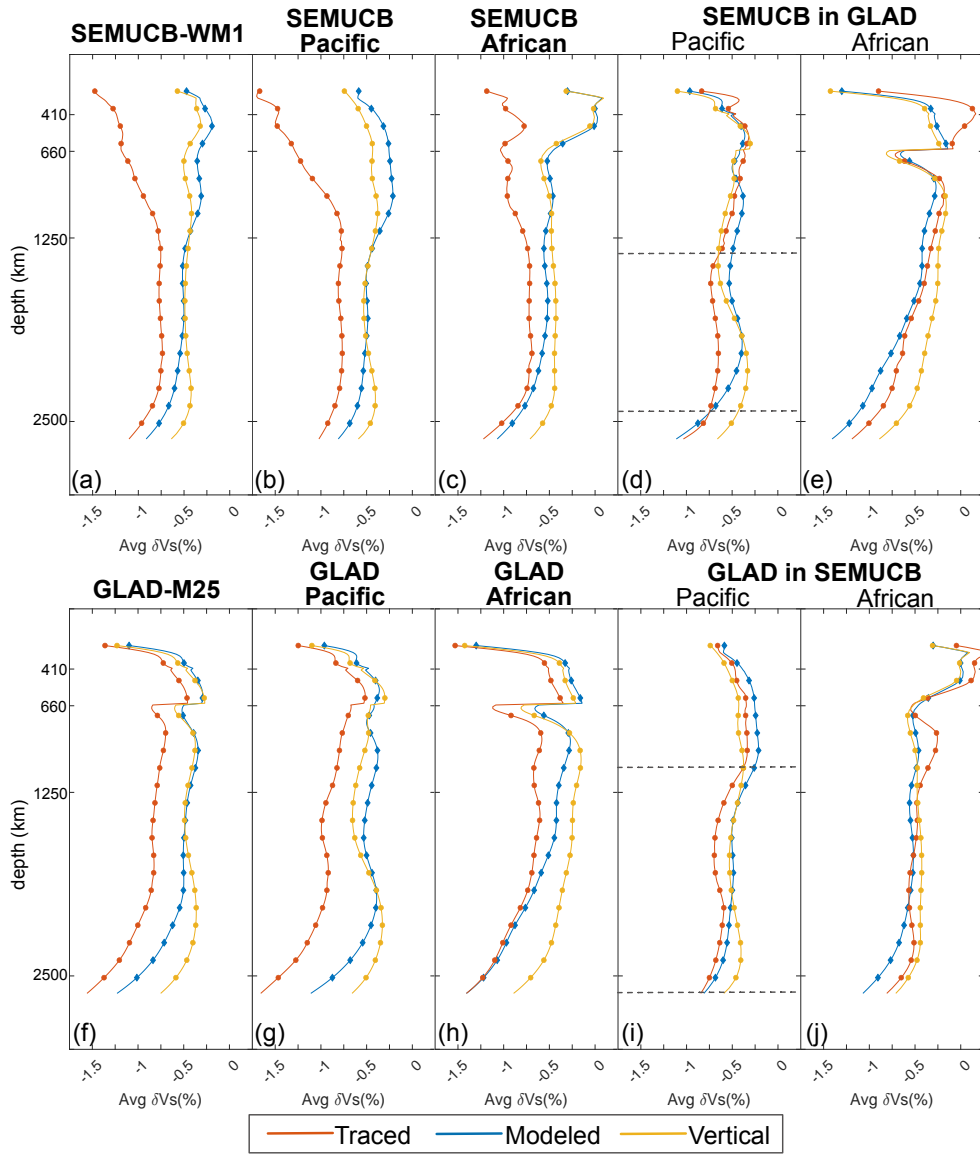


Figure 5. Average δV_S along traced, model-predicted, and vertical plume conduits in two tomographic models. Pacific plumes, which are plumes locate around the Pacific LLSVP, include Caroline, Easter, Galapagos, Hawaii, Macdonald, Marquesas, Pitcairn, Samoa, and Tahiti. African plumes, which are plumes locate around the African LLSVP, include Azores, Canary, Cape Verde, Iceland, Reunion, St. Helena, and Tristan. The dotted lines indicate the depth range where the traced plume conduits from SEMUCB-WM1 (GLAD-M25) outperform either the model-predicted or vertical plume conduits in GLAD-M25 (SEMUCB-WM1).

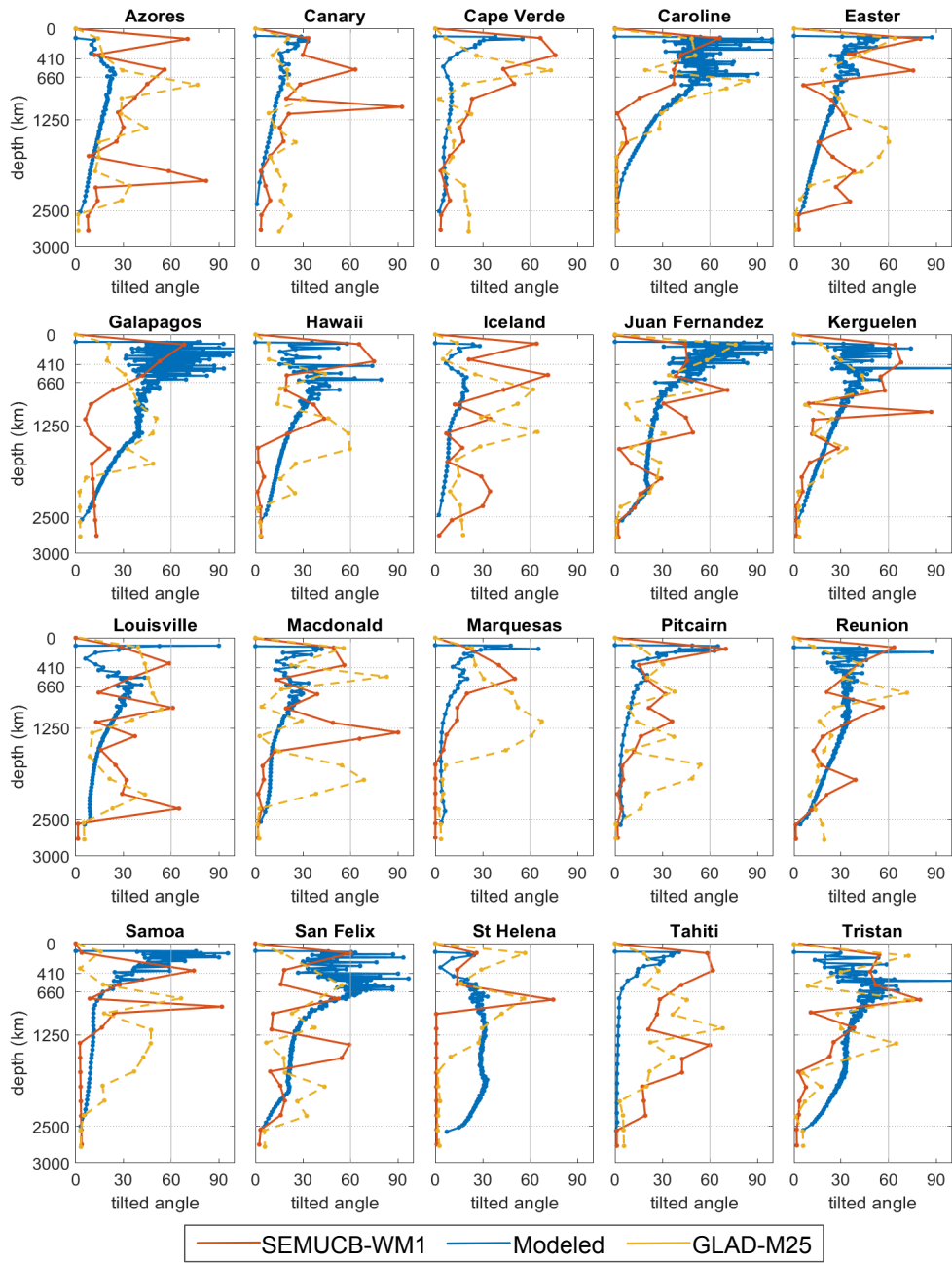


Figure 6. The depth profile of tilt angle along 20 plume conduits. Blue represents the conduits modeled in Steinberger and Antretter (2006). Red represents the traced conduits in SEMUCB-WM1. Yellow represents the traced conduits in GLAD-M25. The gray line marks the 60° angle.

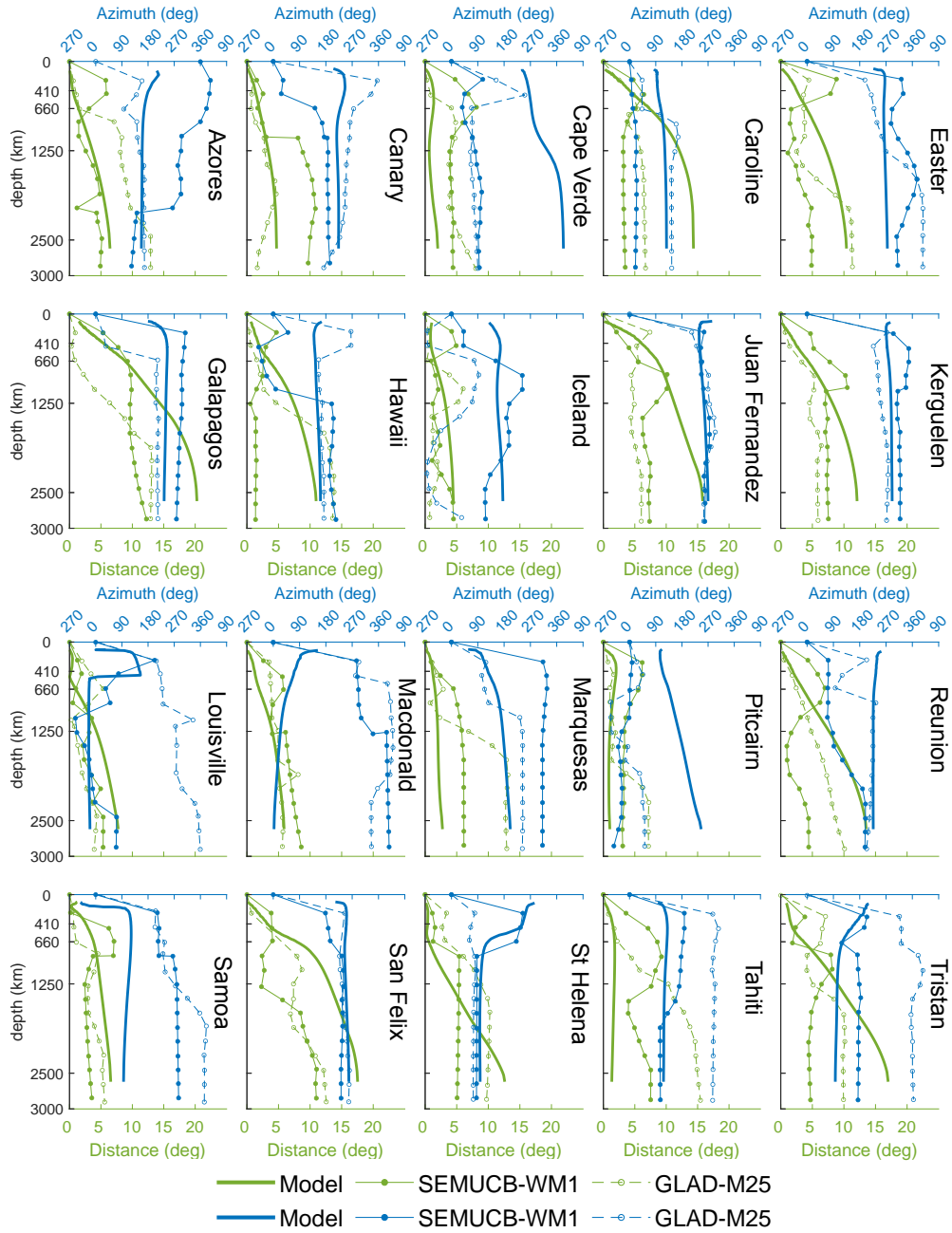


Figure 7. Azimuth and offset distance of model-predicted conduits and conduits traced in SEMUCB-WM1 and GLAD-M25 with respect to hotspots. Blue represents the azimuth of a conduit at different depths. Green represents the angular offset between a conduit and its hotspot.

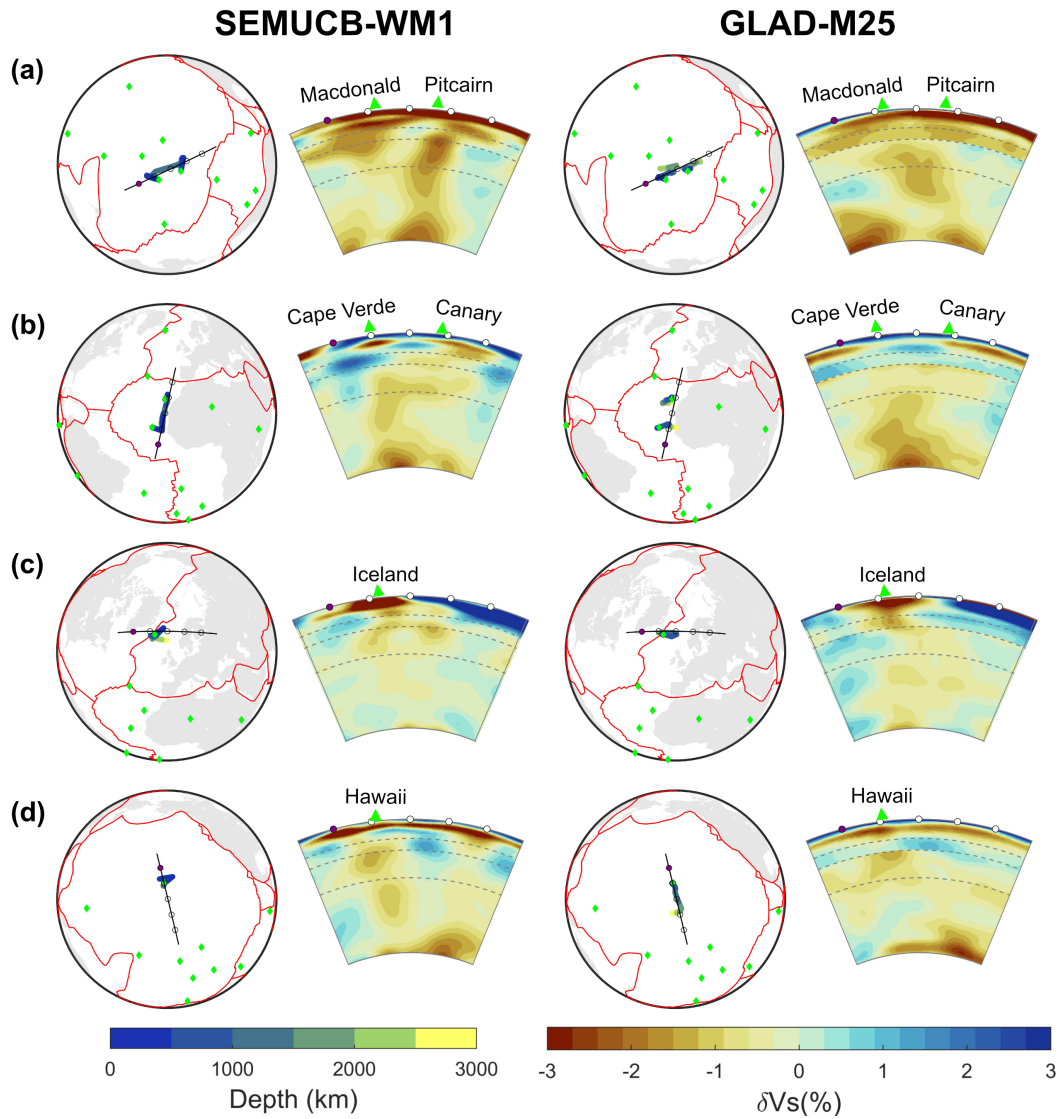


Figure 8. Cross section and map view of the traced conduits of a) Macdonald and Pitcairn, b) Cape Verde and Canary, c) Iceland, d) Hawaii in SEMUCB-WM1 and GLAD-M25. From top to bottom, the dash lines represent 410, 660, and 1250 km depth.

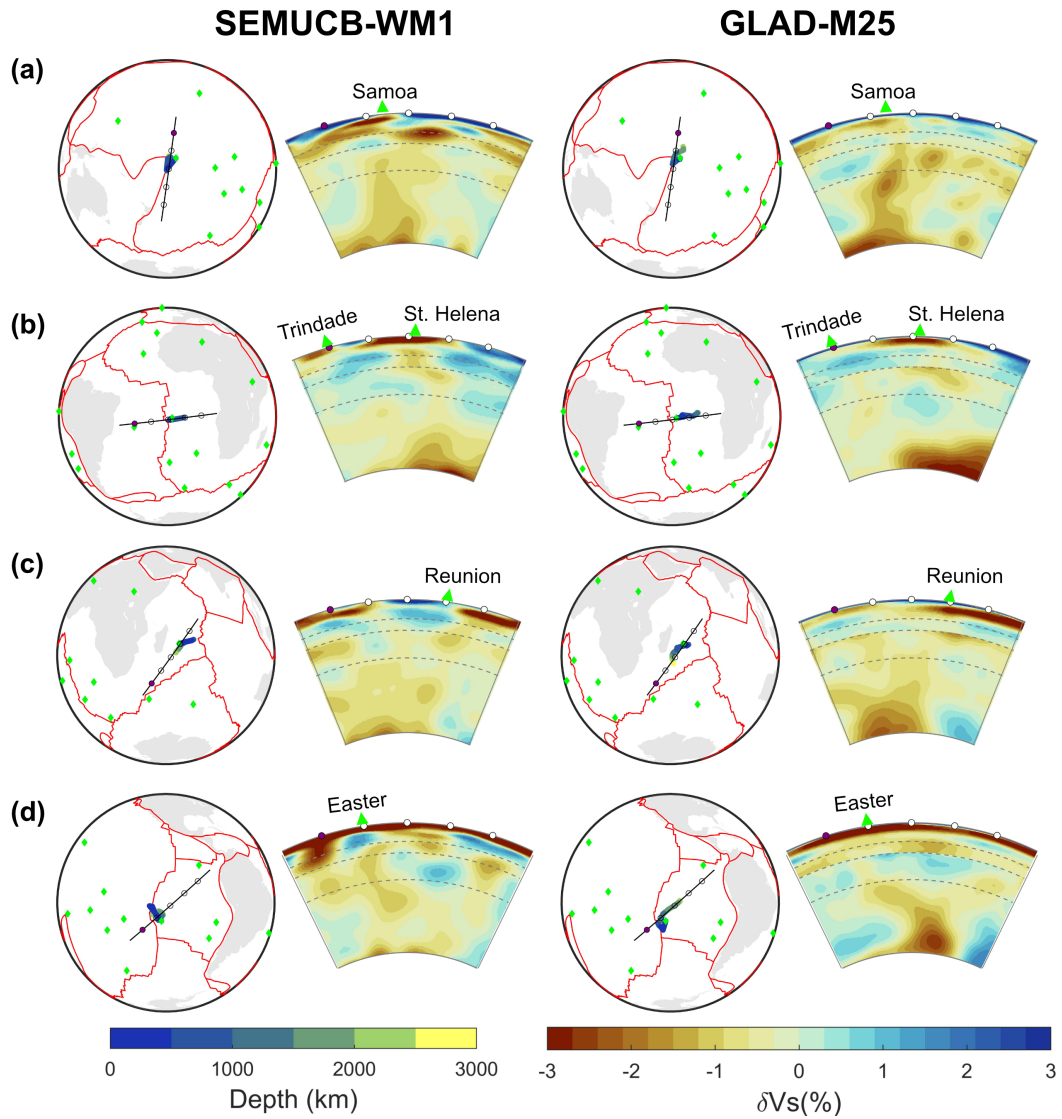


Figure 9. Cross section and map view of the traced conduits of a) Samoa, b) St Helena, c) Reunion, d) Easter similar to Figure 8.

References

- 552
- 553 Ahrens, J., Geveci, B., & Law, C. (2005, January). 36 - ParaView: An End-User
554 Tool for Large-Data Visualization. In C. D. Hansen & C. R. Johnson (Eds.),
555 *Visualization Handbook* (pp. 717–731). Burlington: Butterworth-Heinemann.
556 doi: 10.1016/B978-012387582-2/50038-1
- 557 Austermann, J., Kaye, B. T., Mitrovica, J. X., & Huybers, P. (2014, April). A sta-
558 tistical analysis of the correlation between large igneous provinces and lower
559 mantle seismic structure. *Geophysical Journal International*, *197*(1), 1–9. doi:
560 10.1093/gji/ggt500
- 561 Ballmer, M. D., Schmerr, N. C., Nakagawa, T., & Ritsema, J. (2015, December).
562 Compositional mantle layering revealed by slab stagnation at ~1000-km depth.
563 *Science Advances*, *1*(11), e1500815. doi: 10.1126/sciadv.1500815
- 564 Bao, X., Lithgow-Bertelloni, C. R., Jackson, M. G., & Romanowicz, B. (2022,
565 January). On the relative temperatures of Earth’s volcanic hotspots and
566 mid-ocean ridges. *Science*, *375*(6576), 57–61. doi: 10.1126/science.abj8944
- 567 Bassin, C., Laske, G., & Masters, G. (2000, January). The current limits of resolu-
568 tion for surface wave tomography in North America. *EOS Trans AGU* *81*:F897.
569 *Eos*, *81*, F897.
- 570 Becker, T. W., Schaeffer, A. J., Lebedev, S., & Conrad, C. P. (2015). Toward a
571 generalized plate motion reference frame. *Geophysical Research Letters*, *42*(9),
572 3188–3196. doi: 10.1002/2015GL063695
- 573 Billen, M. I., Kreylos, O., Hamann, B., Jadamec, M. A., Kellogg, L. H., Staadt, O.,
574 & Sumner, D. Y. (2008, September). A geoscience perspective on immersive
575 3D gridded data visualization. *Computers & Geosciences*, *34*(9), 1056–1072.
576 doi: 10.1016/j.cageo.2007.11.009
- 577 Boschi, L., Becker, T. W., & Steinberger, B. (2007). Mantle plumes: Dynamic mod-
578 els and seismic images. *Geochemistry, Geophysics, Geosystems*, *8*(10). doi: 10
579 .1029/2007GC001733
- 580 Brandenburg, J. P., & van Keken, P. E. (2007). Deep storage of oceanic crust in
581 a vigorously convecting mantle. *Journal of Geophysical Research: Solid Earth*,
582 *112*(B6). doi: 10.1029/2006JB004813
- 583 Brunet, D., & Yuen, D. A. (2000, May). Mantle plumes pinched in the transition
584 zone. *Earth and Planetary Science Letters*, *178*(1), 13–27. doi: 10.1016/S0012
585 -821X(00)00063-7
- 586 Celli, N. L., Lebedev, S., Schaeffer, A. J., & Gaina, C. (2021, September). The
587 tilted Iceland Plume and its effect on the North Atlantic evolution and
588 magmatism. *Earth and Planetary Science Letters*, *569*, 117048. doi:
589 10.1016/j.epsl.2021.117048
- 590 Chantel, J., Manthilake, G., Andrault, D., Novella, D., Yu, T., & Wang, Y. (2016,
591 May). Experimental evidence supports mantle partial melting in the astheno-
592 sphere. *Science Advances*, *2*(5), e1600246. doi: 10.1126/sciadv.1600246
- 593 Cordier, C., Delavault, H., & Chauvel, C. (2021, August). Geochemistry of
594 the Society and Pitcairn-Gambier mantle plumes: What they share and
595 do not share. *Geochimica et Cosmochimica Acta*, *306*, 362–384. doi:
596 10.1016/j.gca.2021.04.014
- 597 Courtillot, V., Davaille, A., Besse, J., & Stock, J. (2003, January). Three distinct
598 types of hotspots in the Earth’s mantle. *Earth and Planetary Science Letters*,
599 *205*(3), 295–308. doi: 10.1016/S0012-821X(02)01048-8
- 600 Dannberg, J., & Sobolev, S. V. (2015, April). Low-buoyancy thermochemical plumes
601 resolve controversy of classical mantle plume concept. *Nature Communica-*
602 *tions*, *6*(1), 6960. doi: 10.1038/ncomms7960
- 603 Davaille, A., & Romanowicz, B. (2020). Deflating the LLSVPs: Bundles of Man-
604 tle Thermochemical Plumes Rather Than Thick Stagnant “Piles”. *Tectonics*,
605 *39*(10), e2020TC006265. doi: 10.1029/2020TC006265

- 606 Davies, D. R., Goes, S., & Sambridge, M. (2015, February). On the relationship
 607 between volcanic hotspot locations, the reconstructed eruption sites of large
 608 igneous provinces and deep mantle seismic structure. *Earth and Planetary
 609 Science Letters*, *411*, 121–130. doi: 10.1016/j.epsl.2014.11.052
- 610 Deng, J., & Lee, K. K. M. (2017, December). Viscosity jump in the lower mantle
 611 inferred from melting curves of ferropericase. *Nature Communications*, *8*(11),
 612 1997. doi: 10.1038/s41467-017-02263-z
- 613 Deschamps, F., Cobden, L., & Tackley, P. J. (2012, October). The primitive nature
 614 of large low shear-wave velocity provinces. *Earth and Planetary Science Let-
 615 ters*, *349-350*, 198–208. doi: 10.1016/j.epsl.2012.07.012
- 616 Doubrovine, P. V., Steinberger, B., & Torsvik, T. H. (2016). A failure to reject:
 617 Testing the correlation between large igneous provinces and deep mantle
 618 structures with edf statistics. *Geochemistry, Geophysics, Geosystems*, *17*(3),
 619 1130–1163. doi: 10.1002/2015GC006044
- 620 Faccenda, M., & Dal Zilio, L. (2017, January). The role of solid–solid phase transi-
 621 tions in mantle convection. *Lithos*, *268-271*, 198–224. doi: 10.1016/j.lithos
 622 .2016.11.007
- 623 Farnetani, C. G., & Samuel, H. (2005). Beyond the thermal plume paradigm. *Geo-
 624 physical Research Letters*, *32*(7). doi: 10.1029/2005GL022360
- 625 Ferreira, A. M. G., Faccenda, M., Sturgeon, W., Chang, S.-J., & Schardong, L.
 626 (2019, April). Ubiquitous lower-mantle anisotropy beneath subduction zones.
 627 *Nature Geoscience*, *12*(4), 301–306. doi: 10.1038/s41561-019-0325-7
- 628 French, S. W., Lekic, V., & Romanowicz, B. (2013, October). Waveform tomogra-
 629 phy reveals channeled flow at the base of the oceanic asthenosphere. *Science*,
 630 *342*(6155), 227–230. doi: 10.1126/science.1241514
- 631 French, S. W., & Romanowicz, B. (2015, September). Broad plumes rooted at the
 632 base of the Earth’s mantle beneath major hotspots. *Nature*, *525*(7567), 95–99.
 633 doi: 10.1038/nature14876
- 634 French, S. W., & Romanowicz, B. A. (2014, December). Whole-mantle radi-
 635 ally anisotropic shear velocity structure from spectral-element waveform
 636 tomography. *Geophysical Journal International*, *199*(3), 1303–1327. doi:
 637 10.1093/gji/ggu334
- 638 Hager, B. H. (1984). Subducted slabs and the geoid: Constraints on mantle rhe-
 639 ology and flow. *Journal of Geophysical Research: Solid Earth*, *89*(B7), 6003–
 640 6015. doi: 10.1029/JB089iB07p06003
- 641 Harpp, K. S., & Weis, D. (2020). Insights Into the Origins and Compositions of
 642 Mantle Plumes: A Comparison of Galápagos and Hawai’i. *Geochemistry, Geo-
 643 physics, Geosystems*, *21*(9), e2019GC008887. doi: 10.1029/2019GC008887
- 644 Hassan, R., Flament, N., Gurnis, M., Bower, D. J., & Müller, D. (2015). Provenance
 645 of plumes in global convection models. *Geochemistry, Geophysics, Geosystems*,
 646 *16*(5), 1465–1489. doi: 10.1002/2015GC005751
- 647 He, Y., & Wen, L. (2009). Structural features and shear-velocity structure of the
 648 “Pacific Anomaly”. *Journal of Geophysical Research: Solid Earth*, *114*(B2).
 649 doi: 10.1029/2008JB005814
- 650 Huang, S., Hall, P. S., & Jackson, M. G. (2011, December). Geochemical zoning
 651 of volcanic chains associated with Pacific hotspots. *Nature Geoscience*, *4*(12),
 652 874–878. doi: 10.1038/ngeo1263
- 653 Jackson, M. G., Becker, T. W., & Steinberger, B. (2021). Spatial Characteristics
 654 of Recycled and Primordial Reservoirs in the Deep Mantle. *Geochemistry, Geo-
 655 physics, Geosystems*, *22*(3), e2020GC009525. doi: 10.1029/2020GC009525
- 656 King, S. D., & Adam, C. (2014, October). Hotspot swells revisited. *Physics of the
 657 Earth and Planetary Interiors*, *235*, 66–83. doi: 10.1016/j.pepi.2014.07.006
- 658 King, S. D., & Masters, G. (1992). An inversion for radial viscosity structure using
 659 seismic tomography. *Geophysical Research Letters*, *19*(15), 1551–1554. doi: 10
 660 .1029/92GL01700

- 661 Kumagai, I., Davaille, A., Kurita, K., & Stutzmann, E. (2008). Mantle plumes:
 662 Thin, fat, successful, or failing? Constraints to explain hot spot volcan-
 663 ism through time and space. *Geophysical Research Letters*, *35*(16). doi:
 664 10.1029/2008GL035079
- 665 Kustowski, B., Ekström, G., & Dziewoński, A. M. (2008). Anisotropic shear-wave
 666 velocity structure of the Earth’s mantle: A global model. *Journal of Geophysi-
 667 cal Research: Solid Earth*, *113*(B6). doi: 10.1029/2007JB005169
- 668 Labrosse, S., Hernlund, J. W., & Coltice, N. (2007, December). A crystallizing dense
 669 magma ocean at the base of the Earth’s mantle. *Nature*, *450*(7171), 866–869.
 670 doi: 10.1038/nature06355
- 671 Lei, W., Ruan, Y., Bozdağ, E., Peter, D., Lefebvre, M., Komatitsch, D., . . . Pug-
 672 mire, D. (2020, October). Global adjoint tomography—model GLAD-M25.
 673 *Geophysical Journal International*, *223*(1), 1–21. doi: 10.1093/gji/ggaa253
- 674 Leng, W., & Gurnis, M. (2012). Shape of thermal plumes in a compressible man-
 675 tle with depth-dependent viscosity. *Geophysical Research Letters*, *39*(5). doi:
 676 http://dx.doi.org/10.1029/2012GL050959
- 677 Lewis-Merrill, J., Lo, W. K., Agarwal, K., & Lithgow-Bertelloni, C. R. (2022, De-
 678 cember). Do Mantle Plumes Merge? In *Agu fall meeting abstracts* (Vol. 2022,
 679 p. DI53A-03).
- 680 Liu, C., Yoshino, T., Yamazaki, D., Tsujino, N., Gomi, H., Sakurai, M., . . . Higo,
 681 Y. (2023, August). Effect of water on seismic attenuation of the upper
 682 mantle: The origin of the sharp lithosphere–asthenosphere boundary. *Pro-
 683 ceedings of the National Academy of Sciences*, *120*(32), e2221770120. doi:
 684 10.1073/pnas.2221770120
- 685 Liu, H., & Leng, W. (2020). Plume -Tree Structure Induced by Low-Viscosity Lay-
 686 ers in the Upper Mantle. *Geophysical Research Letters*, *47*(1), e2019GL086508.
 687 doi: 10.1029/2019GL086508
- 688 Marquardt, H., & Miyagi, L. (2015, April). Slab stagnation in the shallow lower
 689 mantle linked to an increase in mantle viscosity. *Nature Geoscience*, *8*(4), 311–
 690 314. doi: 10.1038/ngeo2393
- 691 Matthews, K. J., Maloney, K. T., Zahirovic, S., Williams, S. E., Seton, M., &
 692 Müller, R. D. (2016, November). Global plate boundary evolution and kine-
 693 matics since the late Paleozoic. *Global and Planetary Change*, *146*, 226–250.
 694 doi: 10.1016/j.gloplacha.2016.10.002
- 695 Mitrovica, J. X., & Forte, A. M. (1997). Radial profile of mantle viscosity: Results
 696 from the joint inversion of convection and postglacial rebound observables.
 697 *Journal of Geophysical Research: Solid Earth*, *102*(B2), 2751–2769. doi:
 698 10.1029/96JB03175
- 699 Moses, E., Zocchi, G., Procaccia, I., & Libchaber, A. (1991, January). The Dynam-
 700 ics and Interaction of Laminar Thermal Plumes. *Europhysics Letters*, *14*(1),
 701 55. doi: 10.1209/0295-5075/14/1/010
- 702 Mégnin, C., & Romanowicz, B. (2000, December). The three-dimensional shear
 703 velocity structure of the mantle from the inversion of body, surface and higher-
 704 mode waveforms. *Geophysical Journal International*, *143*(3), 709–728. doi:
 705 10.1046/j.1365-246X.2000.00298.x
- 706 Olson, P., & Kincaid, C. (1991). Experiments on the interaction of thermal convec-
 707 tion and compositional layering at the base of the mantle. *Journal of Geophys-
 708 ical Research: Solid Earth*, *96*(B3), 4347–4354. doi: 10.1029/90JB02530
- 709 Putirka, K. (2008, April). Excess temperatures at ocean islands: Implica-
 710 tions for mantle layering and convection. *Geology*, *36*(4), 283–286. doi:
 711 10.1130/G24615A.1
- 712 Richards, M. A., Duncan, R. A., & Courtillot, V. E. (1989, October). Flood Basalts
 713 and Hot-Spot Tracks: Plume Heads and Tails. *Science*, *246*(4926), 103–107.
 714 doi: 10.1126/science.246.4926.103
- 715 Rudolph, M. L., Lekić, V., & Lithgow-Bertelloni, C. (2015, December). Viscosity

- 716 jump in Earth’s mid-mantle. *Science*, *350*(6266), 1349–1352. doi: 10.1126/
717 science.aad1929
- 718 Shim, S.-H., Grocholski, B., Ye, Y., Alp, E. E., Xu, S., Morgan, D., . . . Prakapenka,
719 V. B. (2017, June). Stability of ferrous-iron-rich bridgmanite under reduc-
720 ing midmantle conditions. *Proceedings of the National Academy of Sciences*,
721 *114*(25), 6468–6473. doi: 10.1073/pnas.1614036114
- 722 Sleep, N. H. (1990). Hotspots and mantle plumes: Some phenomenology.
723 *Journal of Geophysical Research: Solid Earth*, *95*(B5), 6715–6736. doi:
724 10.1029/JB095iB05p06715
- 725 Steinberger, B. (2000). Plumes in a convecting mantle: Models and observations for
726 individual hotspots. *Journal of Geophysical Research: Solid Earth*, *105*(B5),
727 11127–11152. doi: 10.1029/1999JB900398
- 728 Steinberger, B., & Antretter, M. (2006). Conduit diameter and buoyant rising
729 speed of mantle plumes: Implications for the motion of hot spots and shape
730 of plume conduits. *Geochemistry, Geophysics, Geosystems*, *7*(11). doi:
731 10.1029/2006GC001409
- 732 Steinberger, B., & O’Connell, R. J. (1998). Advection of plumes in mantle flow:
733 implications for hotspot motion, mantle viscosity and plume distribution. *Geo-*
734 *physical Journal International*, *132*(2), 412–434. doi: 10.1046/j.1365-246x.1998
735 .00447.x
- 736 Steinberger, B., & Torsvik, T. H. (2012). A geodynamic model of plumes from
737 the margins of Large Low Shear Velocity Provinces. *Geochemistry, Geophysics,*
738 *Geosystems*, *13*(1). doi: 10.1029/2011GC003808
- 739 Tan, E., Leng, W., Zhong, S., & Gurnis, M. (2011). On the location of plumes and
740 lateral movement of thermochemical structures with high bulk modulus in the
741 3-D compressible mantle. *Geochemistry, Geophysics, Geosystems*, *12*(7). doi:
742 10.1029/2011GC003665
- 743 Torsvik, T. H., Smethurst, M. A., Burke, K., & Steinberger, B. (2006, December).
744 Large igneous provinces generated from the margins of the large low-velocity
745 provinces in the deep mantle. *Geophysical Journal International*, *167*(3),
746 1447–1460. doi: 10.1111/j.1365-246X.2006.03158.x
- 747 Tosi, N., & Yuen, D. A. (2011, December). Bent-shaped plumes and horizontal
748 channel flow beneath the 660km discontinuity. *Earth and Planetary Science*
749 *Letters*, *312*(3), 348–359. doi: 10.1016/j.epsl.2011.10.015
- 750 Tsekhmistrenko, M., Sigloch, K., Hosseini, K., & Barruol, G. (2021, August). A
751 tree of Indo-African mantle plumes imaged by seismic tomography. *Nature*
752 *Geoscience*, *14*(8), 612–619. doi: 10.1038/s41561-021-00762-9
- 753 Wamba, M. D., Montagner, J.-P., & Romanowicz, B. (2023, January). Imaging
754 deep-mantle plumbing beneath La Réunion and Comores hot spots: Verti-
755 cal plume conduits and horizontal ponding zones. *Science Advances*, *9*(4),
756 eade3723. doi: 10.1126/sciadv.ade3723
- 757 Wamba, M. D., Montagner, J.-P., Romanowicz, B., & Barruol, G. (2021). Multi-
758 Mode Waveform Tomography of the Indian Ocean Upper and Mid-Mantle
759 Around the Réunion Hotspot. *Journal of Geophysical Research: Solid Earth*,
760 *126*(8), e2020JB021490. doi: 10.1029/2020JB021490
- 761 Wang, W., Walter, M. J., Peng, Y., Redfern, S., & Wu, Z. (2019, August). Con-
762 straining olivine abundance and water content of the mantle at the 410-km
763 discontinuity from the elasticity of olivine and wadsleyite. *Earth and Planetary*
764 *Science Letters*, *519*, 1–11. doi: 10.1016/j.epsl.2019.04.018
- 765 Wang, Y., & Wen, L. (2007). Geometry and P and S velocity structure of the
766 “African Anomaly”. *Journal of Geophysical Research: Solid Earth*, *112*(B5).
767 doi: 10.1029/2006JB004483
- 768 Williams, C. D., Mukhopadhyay, S., Rudolph, M. L., & Romanowicz, B. (2019).
769 Primitive Helium Is Sourced From Seismically Slow Regions in the Lower-
770 most Mantle. *Geochemistry, Geophysics, Geosystems*, *20*(8), 4130–4145. doi:

771 10.1029/2019GC008437

772 Xiang, G., Wang, Z., & Kusky, T. M. (2021, December). Density and viscosity
773 changes between depleted and primordial mantle at ~ 1000 km depth influence
774 plume upwelling behavior. *Earth and Planetary Science Letters*, 576, 117213.
775 doi: 10.1016/j.epsl.2021.117213

776 Zhang, Z., Irving, J. C. E., Simons, F. J., & Alkhalifah, T. (2023, March). Seismic
777 evidence for a 1000 km mantle discontinuity under the Pacific. *Nature Commu-*
778 *nications*, 14(1), 1714. doi: 10.1038/s41467-023-37067-x

779 **Open Research Section**

780 The data and computer code necessary to reproduce all figures is available on Zen-
781 odo (doi: 10.5281/zenodo.10668212). 3D-visualization is done using the Paraview 5.10.0
782 (Ahrens et al., 2005) visualization software.

783 **Acknowledgments**

784 The authors acknowledge support from NSF CSEDI grant EAR-1800450, NSF FRES
785 grant EAR-2317937 and UC Davis. The authors thank reviewer Lapo Boschi, the other
786 anonymous reviewer, the Associate Editor, and Editor for excellent and insightful com-
787 ments and suggestions. The authors thank UC Davis and the KeckCAVES data lab re-
788 siding in this institution for allowing the authors to use the VR headsets in the lab. The
789 authors are grateful of Oliver Kreylos and Sarah King for their assistance with the VR
790 environment. The authors also thank Barbara Romanowicz for helpful discussions about
791 this work.